An iterative multi-atlas patch-based approach for cortex segmentation from neonatal MRI

Carlos Tor Díez, Nicolas Passat, Isabelle Bloch, Sylvain Faisan, Nathalie Bednarek, François Rousseau

An Iterative Multi-Atlas Patch-Based Approach for Cortex Segmentation from Neonatal MRI

Carlos Tor-Díez[a], Nicolas Passat[b], Isabelle Bloch[c], Sylvain Faisan[d],
Nathalie Bednarek[e], François Rousseau[a]

[a]*IMT Atlantique, LaTIM U1101 INSERM, UBL, Brest, France*
[b]*Université de Reims Champagne-Ardenne, CReSTIC, Reims, France*
[c]*LTCI, Télécom ParisTech, Université Paris-Saclay, Paris, France*
[d]*ICube UMR 7357, Université de Strasbourg, CNRS, FMTS, Strasbourg, France*
[e]*Service de médecine néonatale et réanimation pédiatrique, CHU de Reims, France*

Abstract

Brain structure analysis in the newborn is a major health issue. This is especially the case for premature neonates, in order to obtain predictive information related to the child development. In particular, the cortex is a structure of interest, that can be observed in MRI (magnetic resonance imaging). However, neonatal MRI data present specific properties that make them challenging to process. In this context, multi-atlas approaches constitute an efficient strategy, taking advantage of images processed beforehand. The method proposed in this article relies on such multi-atlas strategy. More precisely, it uses two paradigms: first, a non-local model based on patches; second, an iterative optimization scheme. Coupling both concepts allows us to consider patches related not only to the image information, but also to the current segmentation. This strategy is compared to other multi-atlas methods proposed in the literature. Experiments show that the proposed approach provides robust cortex segmentation results.

Keywords: patch-based segmentation, iterative segmentation, neonatal MRI, cortex

1. Introduction

During the last decades, advances in medical imaging have led to their intensive use in clinical routine. This is particularly true for magnetic resonance imaging (MRI), that allows for the acquisition of high-quality images, in a non-ionizing and non-invasive way. At the same time, image processing methods ded-

icated to MRI have increased the informative potential of these data, particularly in the study of brain structures [1].

Most efforts invested in the development of image analysis methods, particularly in segmentation, have focused on brain MRI data of adult subjects. However, MRI data acquired on children and newborns have been the subject of growing interest over the last years. This interest is motivated in particular by the study of early human brain development mechanisms. Thus, it gave rise to the development of specific fields in brain image analysis, on the one hand *in utero* (fetal data) [2, 3], and on the other hand *ex utero* (neonatal data) [4, 5].

Indeed, standard brain segmentation methods and tools, deeply validated for adult MRI data, are generally not adapted to neonatal brain images. In addition to issues related to acquiring MRI data in good conditions (reduced acquisition time, risk of subject motion...), some interpretation difficulties are induced by immaturity of certain brain structures (e.g. partial myelination of the white matter, leading to contrast changes) and, of course, the reduced size of structures of interest.

Brain morphometry is a key tool to assess early brain development and to compute relevant biomarkers [6] that can be further used for diagnosis (for instance through quantitative evaluation of lesions), prediction of motor and cognitive development or therapy (e.g. neuroprotection by melatonin). Neonatal morphometry can also be used to implement a personalized rehabilitative protocol to stimulate brain plasticity [7]. In particular, the cortex is a structure of interest for many recent works focusing on brain folding [8, 9, 10], cortical connectivity [11] and cortical development [12, 13]. However, the cortex is a thin surface object and remains difficult to segment in neonatal MRI data.

Various methods were recently proposed to allow for the segmentation of neonatal brain MRI. From a technical point of view, different approaches were explored: mathematical morphology [14, 15], deformable models [16, 17], classification [18, 19, 20], patch-driven level set approach [21] or probabilistic modelling [22].

Beyond the relative relevance of each of these image processing / machine learning paradigms, another approach that is the so-called multi-atlas framework [23] has demonstrated its interest in the context of brain segmentation. Multi-atlas based techniques are usually performed by registering an anatomy textbook [24] (consisting of one or several labelled images) onto the image to be segmented. The labels are then mapped and fused using classification rules to produce a new label map of the input image. The main items of these registration-based label propagation approaches are the accuracy of the nonrigid registration, the fusion rules,

the selection of the labelled images and the labelling errors in primary manual segmentation. Multi-atlas methods provide a spatial prior that restricts the result to a more realistic anatomy, with the assumption that intensities and segmentation labels are locally correlated. Indeed, by using prior knowledge provided by the anatomy textbook, multi-atlas segmentation techniques can cope with the lower quality of neonates MRI and complexity of the structures of interest [25, 26].

The work presented in this article relies on this multi-atlas strategy. Our purpose is to segment the cortex from 3D MRI data in newborns, considering not only prior appearance information (a given intensity is associated with a given semantics) but also prior spatial information. However, the point-wise mapping conventionally used in multi-atlas approaches, together with the uncertainties induced by the registration step between data, tend to make these prior spatial information less robust.

A possible solution to this issue consists of using the notion of patches, initially introduced for non-local filtering of images [27]. It allows one to take into account not only the value at a point, but also the profile of the values in its neighbourhood, for comparison purpose with the points or neighbourhoods in the other images. This strategy, which can compensate errors and approximations in registration, was used in [28, 29, 30, 31] for brain segmentation. Such algorithm makes use of local similarities between the image to be segmented and the images contained in the anatomy textbook. The principle is similar to a fuzzy block matching approach which avoids the constraint of a strict one-to-one mapping.

In this article, we propose a new way of using patch-based approaches to perform multi-atlas segmentation of the cortex in 3D MRI. Indeed, we propose to use jointly: (1) a patch-based non-local model, and (2) an iterative optimization scheme. The coupled use of these two concepts enables not only to consider patches linked to the image (as in the literature) but also linked to an estimation of its current segmentation. These two kinds of information can be seen similar to the use of data-fidelity and regularisation terms, respectively. This latter regularization ensures a homogeneous behaviour of the segmented structure with regard to its geometry, and the progressive refinement of the result over iterations.

This article is organized as follows. In Section 2 the main principles of multi-atlas segmentation are recalled. Section 3 provides a survey of the main multi-atlas methods for cortical segmentation. Our method is presented in Section 4. A comparative study of the different methods is presented in Section 5. A discussion, proposed in Section 6, concludes the article.

3

2. Multi-atlas segmentation

Contrary to atlas-based segmentation methods, that use a unique probabilistic atlas computed from n images, a *multi-atlas* segmentation method uses directly n segmentation examples. Each such example is obtained from an image, in order to guide the segmentation process of the given input image.

2.1. General approach

The n example images are generally chosen similar (in terms of modality, resolution, observation...) to the input image. Usually, the current image segmentation is then defined as a linear combination of the segmentation information derived from these n examples.

The set $\mathcal{E}$ of the examples is defined as:

$$\mathcal{E} = \{E_i = (I_i, S_i), i = 1 \ldots n\} \tag{1}$$

where each example E_i is composed of one image I_i and its associated segmentation S_i. In our case, I_i is a (grey-level) 3D MRI image that represents a neonate's brain structures. In the associated segmentation S_i, each point y has a value in $[0, 1]$ corresponding to its degree of membership to the chosen structure of interest (in our case, the cortex).

Let I be the input image, and S be the segmentation to be computed from I, thanks to the examples of $\mathcal{E}$. Then, the segmentation S is not simply defined as a function $f(I)$, but more generally as:

$$S = f(I, E_1, \ldots, E_n) \tag{2}$$

Indeed, S depends not only on intrinsic information related to the image I, but also on the way the images I_i are themselves segmented for the same purpose.

This function f is often defined as a linear operator. More precisely, the segmentation S of I is estimated, at each x, as a linear combination of the information gathered in different points y within all other images. In this context, these points y and the weights $w_i(x, y)$ are defined according to the similarity between x in I and y in I_i. The most intuitive way of defining such weights consists of considering them as reversely proportional to the distance between x and y. For instance, such distance can be defined with respect to the intensity information at x and y within their respective images, that is:

$$w_i(x, y) = g(\|I(x) - I_i(y)\|) \tag{3}$$

where g is a function of the distance between $I(x)$ and $I_i(y)$. The segmentation S of I at x can then be defined as a (normalized) linear combination f of the segmentations S_i obtained from the n examples in $\mathcal{E}$:

$$
\begin{aligned}
S(x) &= f(I, E_1, \ldots, E_n)(x) \\
&= \sum_{i=1}^{n} \sum_{y} w_i(x, y) S_i(y)
\end{aligned}
\tag{4}
$$

However, if the similarity measure is computed without considering the spatial context, it will not be robust, in particular to noise and registration errors. Thus, instead of considering the pixel / voxel as comparison unit, some multi-atlas segmentation methods rely on the notion of patch, that is a region within the neighbourhood of each point of interest x. The similarity related to x in the images I_i can then be considered with respect to a richer context.

2.2. Patch-based approaches

For multi-atlas segmentation purposes, using patches as comparison unit requires to define a distance between x in I and y in I_i. Such distance depends on $I(x)$ and $I_i(y)$, but also on the set of the values of I and I_i in the neighbourhoods $P(x)$ and $P(y)$, respectively.

Patches are often defined as isotropic volumes $P(.)$ (squares or cubes of size $2k + 1$) centred on the points of interest. In this framework, the weights $w_i(x, y)$ (Equation (3)) depend on the information carried by the sub-images restricted to the supports of patches:

$$
w_i(x, y) = g \left(\| P_I(x) - P_{I_i}(y)) \| \right)
\tag{5}
$$

In other words, the distance considered for the computation of $w_i(x, y)$ involves the set of point-wise distances, such as defined by Equation (3), on the two patches $P_I(x)$ in I and $P_{I_i}(y)$ in I_i.

Such calculus may be costly, according to the size and number of patches $P(.)$. In order to reduce this computational cost, it is generally chosen to restrict the space of patches for a given point x of I. We only consider the points y located in the neighbourhood $\mathcal{N}(x)$ of x in I_i (of course, a spatial mapping has to be carried out beforehand between I and the images I_i of $\mathcal{E}$; this can be done for instance via a registration step). Under these assumptions, the segmentation S of I rewrites as:

$$
S(x) = \sum_{i=1}^{n} \sum_{y \in \mathcal{N}(x)} w_i(x, y) S_i(y)
\tag{6}
$$

In the next section, the computation of these weights $w_i(x,y)$ is described for different multi-atlas segmentation methods proposed in the literature.

3. Multi-atlas segmentation: Previous works

Following the algorithmic scheme proposed in the survey [23], the multi-atlas methods are composed of three main steps: (1) registration; (2) segmentation propagation; and (3) segmentation fusion.

In the sequel, we focus on step (3) for the principal methods of the literature. In particular, by assuming that segmentation fusion is performed based on Equation (6) (with a normalization coefficient used for making the sum of all weights equal to 1, in each x), the discussion mainly deals with the way of computing the weights $w_i(x,y)$.

3.1. Non-local means

In the pioneering article [27] on Non-Local Means (NLM), the weights considered are calculated according to a Gaussian hypothesis, for denoising purposes. This kind of weights, denoted by w_{NLM}, corresponds to a similarity function reversely proportional to the point-wise intensity distance between the patches, following a normal distribution:

$$w_{NLMi}(x,y) = \exp-\frac{\|P_I(x) - P_{I_i}(y))\|^2}{h^2} \tag{7}$$

where h is a regularization constant that can be automatically tuned [32] as $h = 2\sigma\beta p$ (p, the size of patches), with usually $\beta = 1$, while σ corresponds to the standard deviation of the Gaussian noise in images. By construction, we have $w_{NLMi}(x,y) \in (0,1]$.

3.2. Joint label fusion

The Joint Label Fusion (JLF) method [30], also relies on patches. However, while NLM are first dedicated to denoising, JLF is an algorithm specifically designed for multi-atlas segmentation.

In particular, contrary to NLM, only one patch is selected within the research area $\mathcal{N}(x)$, in order to determine the contribution of an image I_i to the segmentation of I at x. In other words, Equation (6) rewrites as:

$$S(x) = \sum_{i=1}^{n} \hat{w}_i(x)S_i(\hat{y}_i) \tag{8}$$

6

where, for each image I_i, $\hat{y}_i$ is the unique point chosen in $\mathcal{N}(x)$ with respect to the similarity between patches $P_I(x)$ and $P_{I_i}(\hat{y}_i)$. Then, we have:

$$\hat{y}_i = \underset{y \in \mathcal{N}(x)}{\arg\min} \|P_I(x) - P_{I_i}(y)\| \tag{9}$$

Only one weight w_i is then to be computed for each image I_i. Nevertheless, it is defined as spatially variant. In particular, in x, the set $\hat{\mathbf{w}}(x) = \{\hat{w}_i(x), i = 1 \ldots n\}$ is defined as the following minimizer:

$$\hat{\mathbf{w}}(x) = \underset{\mathbf{w}(x) \in W}{\arg\min} \mathbf{w}(x)^t M_x \mathbf{w}(x) \tag{10}$$

where W is the set of vectors $(w_i)_{i=1}^n \in [0,1]^n$ such that $\sum_{i=1}^n w_i = 1$ and M_x is the correlation matrix between the segmentation error probabilities induced by the n images I_i of $\mathcal{E}$ (see [30, Equations (6–12)] for more details).

3.3. Weight optimization

In order to compute the segmentation S of I, determining the weights $w_i(x, y)$ in Equation (6) can also be seen as an optimization problem between the patch of the target image I at point x, and a linear combination of patches of the image I_i in the neighbourhood $\mathcal{N}(x)$.

3.3.1. Optimization on image intensity

This optimization problem can be expressed in the image space. Indeed, one can set the energy function:

$$\phi_I(x) = \left\| P_I(x) - \sum_{i=1}^n \sum_{y \in \mathcal{N}(x)} w_i(x, y) P_{I_i}(y) \right\| \tag{11}$$

that defines the distance between the patch $P_I(x)$ estimated in the image I in the neighbourhood of x, and the linear combination of the patches $P_{I_i}(y)$ in I_i for all the y of $\mathcal{N}(x)$.

The minimization of $\phi_I(x)$ allows us to obtain the weights $\hat{\mathbf{w}}(x) = \{w_i(x, y) \mid y \in \mathcal{N}(x), i = 1 \ldots n\}$:

$$\hat{\mathbf{w}}(x) = \underset{\mathbf{w} \in W}{\arg\min} \phi_I(x) \tag{12}$$

where W is the set of normalized vectors taking their values in $[0, 1]$.

This approach is inspired from the LLE (Locally Linear Embedding) algorithm [33], initially designed for dimension reduction purposes.

3.3.2. Optimization on segmentation

The above strategy can also be considered in the space of segmentations. To this end, it is then necessary to replace, in the definition of $\phi_I(x)$ (Equation (11)), the patches P_I and P_{I_i} on images I and I_i by the patches P_S and P_{S_i} on the segmentations S and S_i associated to these images.

The same optimization scheme (Equation (12)) can then be used for determining the weights $\hat{\mathbf{w}}(x) = \{w_i(x, y) \mid y \in \mathcal{N}(x), i = 1 \ldots n\}$.

This formulation requires to know beforehand the segmentation S of the target image I. Thus, it mainly presents a retrospective interest, in particular for comparing results. Nevertheless, as discussed hereafter, it can also be useful in the context of iterative optimization schemes.

4. Iterative optimization

Our proposed approach is dedicated to patch-based multi-atlas segmentation. It essentially relies on the optimization scheme presented in Section 3.3. Its two main principles are the following.

On the one hand, the proposed optimization scheme is iterative. In particular, the computed weights $w_i(x, y)$ can evolve in order to converge progressively towards a satisfactory solution. On the other hand, contrary to the formulation proposed in Equations (11–12), the optimization does no longer rely only on data-fidelity, but also on the current segmentation. In other words, the evolution of the weights $w_i(x, y)$ are guided by two kinds of information: proximity between patches in the image space, and proximity in segmentation space.

4.1. Mixed patches

In particular, we propose to define mixed patches $P_{E_\star}$ from image–segmentation couples $E_\star = (I_\star, S_\star)$.

All the considered images $I_\star$ (namely, I and the I_i) are defined on a same support Ω (indeed, they were registered beforehand), and they take their values within an interval $V \subset \mathbb{R}$. The associated segmentations $S_\star$ are defined on the same support Ω, but they take their values in $[0, 1]$. Without loss of generality, we consider that V has been normalized. Under these assumptions, both the $I_\star$ and the $S_\star$ can be expressed as functions $\Omega \to [0, 1]$ (with, however, distinct semantics). This normalization is crucial for defining a non-biased inter-patch distance.

8

Practically, for an image–segmentation couple $E_\star = (I_\star, S_\star)$, the space of associated patches $E_\star$ is a function:

$$\left| \begin{array}{rcl} P_{E_\star} & : & \Omega \rightarrow [0,1]^p \times [0,1]^p \\ & & x \mapsto (P_{I_\star}(x), P_{S_\star}(x)) \end{array} \right. \tag{13}$$

where $P_{I_\star}(x)$ and $P_{S_\star}(x)$ are the usual patches of image and segmentation, respectively, that is vectors of $[0,1]^p$, that indicate the values of $I_\star$ and $S_\star$ inside a window $\mathcal{N}(x)$ of Ω of size p, locally centred on x. (For the sake of concision, we will equivalently consider $P_{E_\star}(x)$ as a vector $(p_{E_\star}^k(x))_{k=1}^{2p}$ of $[0,1]^{2p}$ instead of a couple of vectors of size p.)

4.2. Inter-patch distance and energy function

In order to define the inter-patch distance, the L_k norms (and especially L_1 and L_2) can be considered:

$$\|P_{E_\alpha}(x) - P_{E_\beta}(x)\|_1 = \sum_{k=1}^{2p} \left| p_{E_\alpha}^k(x) - p_{E_\beta}^k(x) \right| \tag{14}$$

$$\|P_{E_\alpha}(x) - P_{E_\beta}(x)\|_2 = \left(\sum_{k=1}^{2p} \left(p_{E_\alpha}^k(x) - p_{E_\beta}^k(x) \right)^2 \right)^{\frac{1}{2}} \tag{15}$$

In particular, it is possible to define, in a way similar to Equation (11), an energy function ϕ_E which, given a image–segmentation couple $E = (I, S)$ and a multi-atlas set $\mathcal{E} = \{E_i = (I_i, S_i), i = 1 \ldots n\}$, expresses the distance between E and a linear combination on $\mathcal{E}$ at a point x of Ω:

$$\phi_E(x) = \left\| P_E(x) - \sum_{i=1}^n \sum_{y \in \mathcal{N}(x)} w_i(x,y) P_{E_i}(y) \right\| \tag{16}$$

The purpose then consists of determining the weights $w_i(x,y)$ allowing one to minimize this function.

4.3. Optimization scheme

As in Equation (12), our purpose is to minimize the function $\phi_E(x)$ in order to obtain a vector of optimal weights for computing the segmentation S of I at x:

$$\hat{\mathbf{w}}(x) = \arg\min_{\mathbf{w} \in W} \phi_E(x) \tag{17}$$

Algorithm 1 Iterative optimization algorithm

Require: I: input image ; $\mathcal{E} = \{E_i = (I_i, S_i), i = 1 \dots n\}$: multi-atlas ; N: number of iterations

Ensure: S: segmentation of I

1: **for** $j = 0 \dots N - 1$ **do**
2:     **for all** $x \in \Omega$ **do**
3:         Compute $\hat{\mathbf{w}}^{(j)}(x)$ (Equation (18))
4:         Compute $S^{(j)}(x)$ from $\hat{\mathbf{w}}^{(j)}(x)$ (Equation. (19))
5:     **end for**
6: **end for**
7: $S \leftarrow S^{(N-1)}$

---

with the same notations as in Section 3.3.

In particular, the same optimization scheme can be used. However, the strategy is now iterative. Algorithm 1 summarizes the overall method. Its successive steps are discussed hereafter.

4.3.1. Initialization

The first iteration of the process requires to define beforehand an initial image–segmentation couple $E^{(-1)} = (I, S^{(-1)})$ associated to I. The initial segmentation $S^{(-1)}$ can be chosen arbitrarily. This initialization is justified hereafter, in the weighting policy description.

4.3.2. Iterations

At the j-th stage of the iterative process, the current energy function $\phi_E^{(j)}(x)$ is optimized by considering $P_E^{(j-1)}(x) = (P_I(x), P_{S^{(j-1)}}(x))$, in order to define the weights $w_i^{(j)}(x, y)$ (Equations (16–17)):

$$\hat{\mathbf{w}}^{(j)}(x) = \arg\min_{\mathbf{w} \in W} \left\| P_E^{(j-1)}(x) - \sum_{i=1}^{n} \sum_{y \in \mathcal{N}(x)} w_i(x, y) P_{E_i}(y) \right\| \tag{18}$$

and then to compute $S^{(j)}$ from these weights $w_i^{(j)}(x, y)$ of $\hat{\mathbf{w}}^{(j)}(x)$:

$$S^{(j)}(x) = \sum_{i=1}^{n} \sum_{y \in \mathcal{N}(x)} w_i^{(j)}(x, y) S_i(y) \tag{19}$$

10

4.3.3. Weighting

We propose to weight the influence of the terms related to intensity and estimated segmentation, respectively. Here, the underlying idea is to relax progressively the hypothesis of isometry between intensity space and segmentation space.

In particular, at each iteration j, we consider a parameter $\alpha_j \in [0, 1]$ such that the terms of $P_{E_\star}$ linked to the patch $P_{S_\star}$ (resp. $P_{I_\star}$) are weighted by α_j (resp. $1 - \alpha_j$).

Practically, this weighting can be realized without altering the formulation of Equations (17–19). Indeed, it is sufficient that the α_j weights be involved in the definition of $P_{E_\star}$ by applying a scale function onto the value space. In other words, we define a function:

$$\left| \begin{array}{cccc} \Pi_\alpha & : & [0, 1]^p \times [0, 1]^p & \rightarrow & \mathbb{R}^p \times \mathbb{R}^p \\ & & (P_{I_\star}, P_{S_\star}) & \mapsto & ((1 - \alpha)P_{I_\star}, \alpha P_{S_\star}) \end{array} \right. \tag{20}$$

It is then sufficient to substitute $\Pi_{\alpha_j} \circ P_{E_\star}$ to $P_{E_\star}$ in the above optimization scheme. In order to guarantee a continuous evolution of the process, we choose an increasing sequence of weights (α_j) depending on j. At the first iteration, α_0 is set to 0. Then any initialization of the segmentation $S^{(-1)}$ can be considered.

4.3.4. Termination

The iterative process ends when a given number N of iterations has been performed. This value N can be defined manually. (If the number of required iterations is unknown a priori, the termination may alternatively be handled by considering a convergence criterion.)

5. Experiments

In this section, we apply the proposed method for processing 3D neonates cerebral MRI images. Our purpose is to segment cortical structures from these data, by taking advantage of a base of similar images, endowed with segmentations.

5.1. Data

The considered images are T2-weighted MRIs, made available [34] in the context of the Developing Human Connectome Project (dHCP)[1] [35], and provided by the Evelina Neonatal Imaging Centre, London, UK.

---

[1]http://www.developingconnectome.org

The subjects are aged between 37–44 weeks. The data were acquired on a 3T Achieva scanner, dedicated to neonates, with an acquisition time of approximately 60 minutes. The size of voxels is $0,5 \times 0,5 \times 0,5$ mm^3. The repetition (TR) and echo times (TE) are $12\,000$ and 156 ms, respectively.

A set of 40 images is considered. Among these data, 30 are used for building an example dataset (multi-atlas: I_i), while the other 10 are used as input images (I). For each of these 40 images, the algorithmic pipeline dHCP[2] has been applied. The obtained segmentations, visually validated, constitute our reference. For the 30 images I_i, they provide us with the segmentations S_i; for the 10 images I, they provide us with the expected segmentations S.

5.2. Data preprocessing

The example images were registered in two steps (affine, then non-rigid registration) by using ANTs[3] [36]. In order to make patch-based methods robust, the intensities of example images (I_i) were normalized by histogram matching with the subjects to be segmented (I). This is done in order to avoid additive bias effects on inter-patch distances (Equations (14–15)).

5.3. Compared methods

The proposed method, described in Section 4, and denoted by ITER in the sequel, was compared to the following methods:

- Non-Local Means – NLM [27] (Section 3.1);

- Joint Label Fusion – JLF [30] (Section 3.2);

- MANTIS [18].

It is worth mentioning that the first two are patch-based multi-atlas methods, such as to ITER. By contrast, MANTIS is not multi-atlas; it is based on classification principles. Indeed, this latter method relies on an adaptation of the unified segmentation algorithm [37], enriched with morphological processing and topological filtering steps.

---

[2]https://github.com/DevelopingHCP/structural-pipeline
[3]http://stnava.github.io/ANTs

5.4. Parameters

The MANTIS method presents few parameters. These are regularization parameters for the initial classification of the unified segmentation [37]. The used values are those defined by default.

The other methods based on patches all present similar characteristics. In particular, they share various parameters: the number K of nearest neighbours among $\mathcal{N}(.)$, considered for the calculus of energy functions $\phi(.)$ (Equation (11) and next); the size p of the patches $P(.)$; and the dimension of research areas $\mathcal{N}(.)$.

The use of the K nearest neighbours among $n.|\mathcal{N}(x)|$ for the calculus of $\phi(x)$ is aimed to reduce the influence of an excessive amount of patches with a low similarity with the considered patch in each point $x \in \Omega$. The parameter K is fixed to 15, except for JLF where, by definition, we have $K = n$ (here, 30). The value of p is set to 27; it corresponds to patches of size $3 \times 3 \times 3$ voxels. The research areas $\mathcal{N}(.)$ are cubes with $7 \times 7 \times 7$ voxels. These parameters were set based on preliminary experiments.

Some parameters are specific to some of these methods. In JLF, the supplementary parameters were set at a fixed default value. For the ITER method, the inter-patch distance relies on the L_2 norm (Equation (15)). The regularization parameter for inversion is set to 10^{-3}. The number of iterations N was empirically set to 2. The values of α_j (trade-off coefficient) are set to 0 and 0.25 for the first and second iteration, respectively. The 0 value allows us at perform a first iteration based on data-fidelity only. The 0.25 value for the second iteration was determined from preliminary experiments, within a range of values from 10^{-2} to 0.5. The K nearest neighbours are updated at each iteration. This allows us to combine examples that are increasingly adapted to estimate the segmentation, according to the evolution of α_j.

6. Results and discussion

6.1. Results

Quantitative evaluations of the results provided by the four methods are gathered in Table 1. In particular, two evaluation measures were considered: the Dice index and the Peak Signal to Noise Ratio (PSNR). The Dice index (that varies between 0 and 1) is an overlapping measure between the estimated segmentation and the ground-truth; the closer to 1, the better the adequacy between the result and the ground-truth both in terms of false positives and false negatives. The PSNR

Table 1: Performances of ITER, compared to three other segmentation methods (NLM, JLF, MANTIS) applied on 10 subjects, with an example base of 30 subjects.

	NLM [27]	JLF [30]	MANTIS [18]	ITER
Dice (mean)	0,876	0,845	0,793	0,887
Dice (std. dev.)	0,011	0,018	0,028	0,011
PSNR (mean, dB)	20,758	18,966	16,661	21,086
PSNR (std. dev., dB)	0,396	0,487	0,533	0,392

provides a measure of quality (mean quadratic error) of the estimated image; the higher its value (in dB), the better the quality of the obtained result.

The ITER and NLM methods generate results defined as fuzzy maps. In order to compare these results with those of JLF and MANTIS (that generate binary maps), a thresholding of the fuzzy maps is set at value 0.5.

A more qualitative assessment of the results obtained by the four method is also available via illustrative samples of segmentations, visualized on 2D slices, in Figures 1–2 (axial slices), and as 3D visualizations of meshed obtained from binary volumes (sagittal view) in Figure 3 and using tools from BrainVISA software[4] [38].

6.2. *Discussion and perspectives*

From a quantitative point of view (Table 1), the results obtained with ITER are better than those obtained with the other three tested methods. This is verified for both Dice and PSNR measures. This improvement is significant compared to the JLF and MANTIS methods; it is lower compared to the NLM method (approximately 0.01 gap for Dice and 0.3 dB for PSNR). These first results tend to show that the proposed strategy of coupling patch-based and iterative optimization indeed makes sense, as the results are at the level of the state of the art. In addition to this algorithmic approach, the simultaneous use of a data-fidelity term and a regularization term from both the example images and their segmentations in same patches, also seems relevant. Indeed, compared to ITER, the NLM method, although being also patch-based, is neither iterative nor image/segmentation mixing.

---

[4]http://brainvisa.info

Despite slight quantitative differences between ITER and the other methods, observation of the visual results confirms the satisfactory behaviour of the ITER method from a more qualitative point of view. First, this can be seen on 2D slices in Figures 1–2. In Figure 1, one can observe that MANTIS clearly oversegments the cortex, compared to the other three methods, while JLF tends to slightly undersegment it. ITER and NLM provide visually comparable results, with slightly more noisy results for NLM. These trends are confirmed by Figure 2, where we can focus on a zoomed area of the slice, and observe the zones of false positives and false negatives. This illustration emphasizes the over- and undersegmentation behaviours of MANTIS and JLF, respectively. Once again, NLM and ITER provide close results, but ITER seems to present lower false negatives.

Second, the behaviour of the four methods can be qualitatively observed from 3D cortical surfaces computed based on segmentation results. Indeed, in Figure 3, one can observe that JLF leads to topologically incorrect surfaces (holes), due to undersegmentation, while the oversegmentation of MANTIS leads to noisy patterns on the surface, and disconnected elements. Once again, NLM and ITER provide globally correct surfaces, with a slightly more regular appearance with ITER.

Overall, these experiment argue in favour of considering mixed patches and iterative optimization schemes for patch-based segmentation approaches. This is, in particular, strengthened by the fact that these results were obtained in a complicated applicative context, namely the analysis of cortical structures.

However, these results are yet preliminary. At this stage, they cover a small data set of 10 + 30 images. In addition, these data present good contrast quality and signal-to-noise ratio. Consequently, it will be mandatory to assess the robustness of ITER in more challenging contexts, with data of lower quality.

In addition, since the method is based on a multi-atlas paradigm, it may be relevant to investigate the impact of example quality, in order to understand the side effects of imperfect segmentation examples, but also heterogeneous data collected in multi-centric studies.

Finally, the space of parameters of the ITER method has not been fully explored. In particular, the type of distance, the number of closest neighbours, the weighting policies will deserve a wider study. We will also consider larger ranges of iterations, in order to observe if smooth evolutions of the trade-off parameter α could enable to improve the overall quality of the segmentation results.
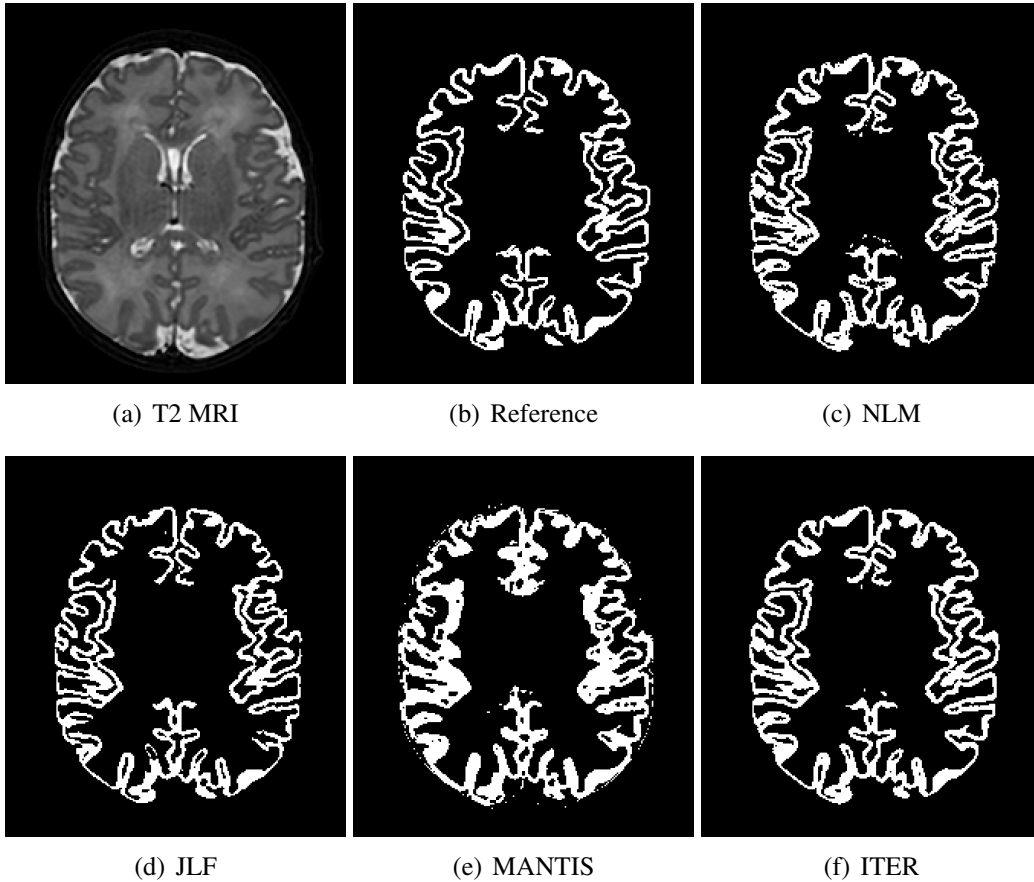
Figure 1: Segmentation results on a T2-weighted brain MRI (axial slice). (a) Input image. (b) Reference segmentation obtained from the dHCP pipeline [17]. Segmentation results obtained with: (c) NLM [27], (d) JLF [30], (e) MANTIS [18], (f) ITER.

Acknowledgements

[1] A. W. Toga, Brain Mapping: An Encyclopedic Reference, Academic Press, 2015.

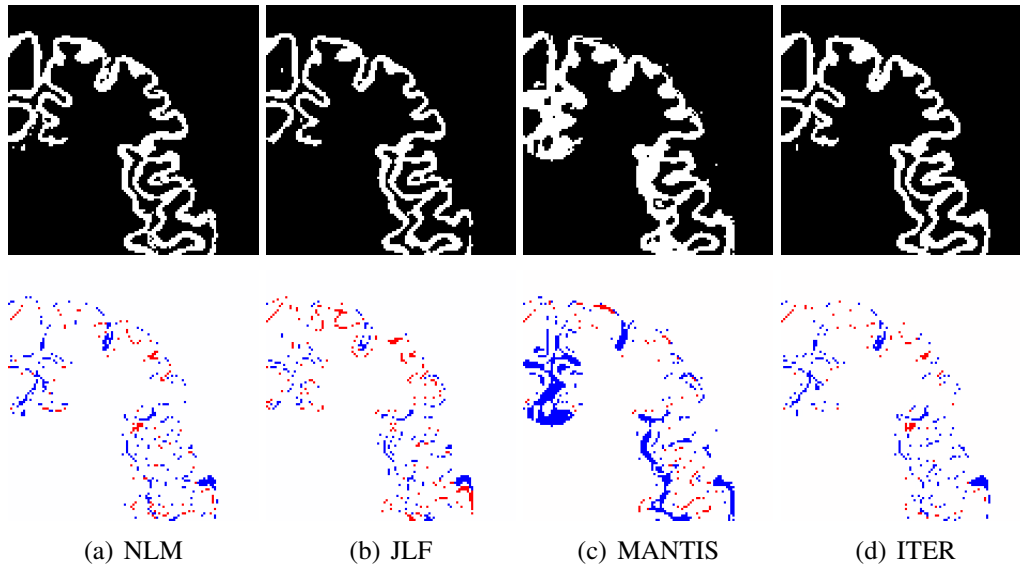[2] F. Rousseau, C. Studholme, R. Jardri, M. Thomason, In vivo human fe-

Figure 2: First row: zoom on a region of Figure 1. Second row: false positives (in blue) and false negatives (in red) provided by the different methods, compared to the reference image (Figure 1(b)). (a) NLM [27], (b) JLF [30], (c) MANTIS [18], (d) ITER.

tal brain analysis using MR imaging, in: Fetal Development: Research on Brain and Behavior, Environmental Influences, and Emerging Technologies, Springer International Publishing, pp. 407–427.

[3] O. M. Benkarim, G. Sanroma, V. A. Zimmer, E. Muñoz-Moreno, N. Hahner, E. Eixarch, O. Camara, M. A. González Ballester, G. Piella, Toward the automatic quantification of in utero brain development in 3D structural MRI: A review, Human Brain Mapping 38 (2017) 2772–2787.

[4] C. N. Devi, A. Chandrasekharan, V. K. Sundararaman, Z. C. Alex, Neonatal brain MRI segmentation: A review, Computers in Biology and Medicine 64 (2015) 163–178.

[5] A. Makropoulos, S. J. Counsell, D. Rueckert, A review on automatic fetal and neonatal brain MRI segmentation, NeuroImage 170 (2018) 231–248.

[6] L. R. Ment, D. Hirtz, P. S. Hüppi, Imaging biomarkers of outcome in the developing preterm brain, The Lancet Neurology 8 (2009) 1042–1055.

[7] P. S. Hüppi, Cortical development in the fetus and the newborn: Advanced
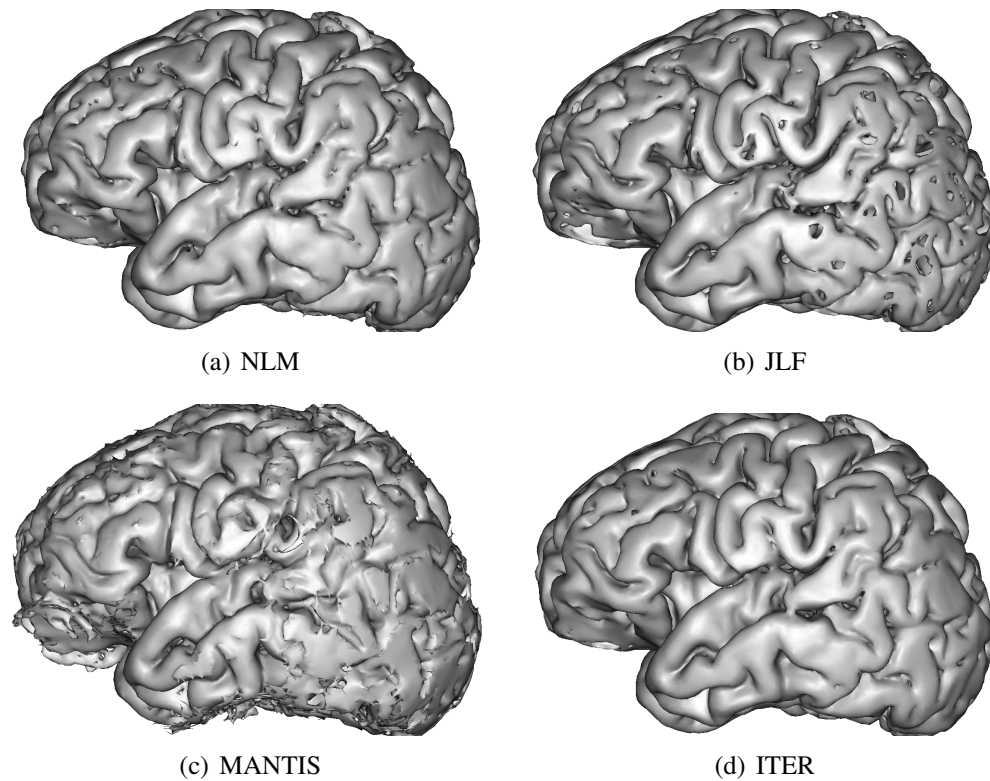
(a) NLM

(b) JLF

(c) MANTIS

(d) ITER

Figure 3: 3D visualization of mesh surfaces computed from the segmentation results obtained with (a) NLM [27], (b) JLF [30], (c) MANTIS [18], (d) ITER.

MR techniques, Topics in Magnetic Resonance Imaging: TMRI 22 (2011) 33–38.

[8] J. Dubois, M. Benders, A. Cachia, F. Lazeyras, R. Ha-Vinh Leuchter, S. V. Sizonenko, C. Borradori-Tolsa, J. F. Mangin, P. S. Hüppi, Mapping the early cortical folding process in the preterm newborn brain, Cerebral Cortex 18 (2008) 1444–1454.

[9] J. Lefèvre, D. Germanaud, J. Dubois, F. Rousseau, I. de Macedo Santos, H. Angleys, J.-F. Mangin, P. S. Hüppi, N. Girard, F. De Guio, Are developmental trajectories of cortical folding comparable between cross-sectional datasets of fetuses and preterm newborns?, Cerebral Cortex 26 (2016) 3023–3035.

[10] E. Orasanu, A. Melbourne, M. J. Cardoso, H. Lomabert, G. S. Kendall, N. J. Robertson, N. Marlow, S. Ourselin, Cortical folding of the preterm brain: A longitudinal analysis of extremely preterm born neonates using spectral matching, Brain and Behavior 6 (2016).

[11] G. Ball, J. P. Boardman, P. Aljabar, A. Pandit, T. Arichi, N. Merchant, D. Rueckert, A. D. Edwards, S. J. Counsell, The influence of preterm birth on the developing thalamocortical connectome, Cortex 49 (2013) 1711–1721.

[12] G. Ball, L. Srinivasan, P. Aljabar, S. J. Counsell, G. Durighel, J. V. Hajnal, M. A. Rutherford, A. D. Edwards, Development of cortical microstructure in the preterm human brain, Proceedings of the National Academy of Sciences of the United States of America 110 (2013) 9541–9546.

[13] Q. Yu, A. Ouyang, L. Chalak, T. Jeon, J. Chia, V. Mishra, M. Sivarajan, G. Jackson, N. Rollins, S. Liu, H. Huang, Structural development of Human fetal and preterm brain cortical plate based on population-averaged templates, Cerebral Cortex 26 (2016) 4381–4391.

[14] L. Gui, R. Lisowski, T. Faundez, P. S. Hüppi, F. Lazeyras, M. Kocher, Morphology-driven automatic segmentation of MR images of the neonatal brain, Medical Image Analysis 16 (2012) 1565–1579.

[15] B. Morel, Y. Xu, A. Virzi, T. Géraud, C. Adamsbaum, I. Bloch, A challenging issue: Detection of white matter hyperintensities in neonatal brain MRI, in: EMBC, Procs., 2016, pp. 93–96.

[16] F. Leroy, J.-F. Mangin, F. Rousseau, H. Glasel, L. Hertz-Pannier, J. Dubois, G. Dehaene-Lambertz, Atlas-free surface reconstruction of the cortical grey-white interface in infants, PloS One 6 (2011) e27128.

[17] A. Schuh, A. Makropoulos, R. Wright, E. C. Robinson, N. Tusor, J. Steinweg, E. Hughes, L. C. Grande, A. Price, J. Hutter, J. V. Hajnal, D. Rueckert, A deformable model for the reconstruction of the neonatal cortex, in: ISBI, Procs., 2017, pp. 800–803.

[18] R. J. Beare, J. Chen, C. E. Kelly, D. Alexopoulos, C. D. Smyser, C. E. Rogers, W. Y. Loh, L. G. Matthews, J. L. Y. Cheong, A. J. Spittle, P. J. Anderson, L. W. Doyle, T. E. Inder, M. L. Seal, D. K. Thompson, Neonatal

brain tissue classification with morphological adaptation and unified segmentation, Frontiers in Neuroinformatics 10 (2016) 12.

[19] P. Moeskops, M. J. Benders, S. M. Chiţă, K. J. Kersbergen, F. Groenendaal, L. S. de Vries, M. A. Viergever, I. Išgum, Automatic segmentation of MR brain images of preterm infants using supervised classification, NeuroImage 118 (2015) 628–641.

[20] P. Anbeek, I. Išgum, B. J. M. van Kooij, C. P. Mol, K. J. Kersbergen, F. Groenendaal, M. A. Viergever, L. S. d. Vries, M. J. N. L. Benders, Automatic segmentation of eight tissue classes in neonatal brain MRI, PLOS ONE 8 (2013) e81895.

[21] L. Wang, F. Shi, G. Li, Y. Gao, W. Lin, J. H. Gilmore, D. Shen, Segmentation of neonatal brain MR images using patch-driven level sets, NeuroImage 84 (2014) 141–158.

[22] M. J. Cardoso, A. Melbourne, G. S. Kendall, M. Modat, N. J. Robertson, N. Marlow, S. Ourselin, AdaPT: An adaptive preterm segmentation algorithm for neonatal brain MRI, NeuroImage 65 (2013) 97–108.

[23] J. E. Iglesias, M. R. Sabuncu, Multi-atlas segmentation of biomedical images: A survey, Medical Image Analysis 24 (2015) 205–219.

[24] M. I. Miller, G. E. Christensen, Y. Amit, U. Grenander, Mathematical textbook of deformable neuroanatomies, Proceedings of the National Academy of Sciences of the United States of America 90 (1993) 11944–11948.

[25] A. Makropoulos, I. S. Gousias, C. Ledig, P. Aljabar, A. Serag, J. V. Hajnal, A. D. Edwards, S. J. Counsell, D. Rueckert, Automatic whole brain MRI segmentation of the developing neonatal brain, IEEE Transactions on Medical Imaging 33 (2014) 1818–1831.

[26] N. I. Weisenfeld, S. K. Warfield, Automatic segmentation of newborn brain MRI, NeuroImage 47 (2009) 564–572.

[27] A. Buades, B. Coll, J. Morel, A review of image denoising algorithms, with a new one, Multiscale Modeling & Simulation 4 (2005) 490–530.

[28] F. Rousseau, P. A. Habas, C. Studholme, A supervised patch-based approach for human brain labeling, IEEE Transactions on Medical Imaging 30 (2011) 1852–1862.

20

[29] P. Coupé, J. V. Manjón, V. Fonov, J. Pruessner, M. Robles, D. L. Collins, Patch-based segmentation using expert priors: Application to hippocampus and ventricle segmentation, NeuroImage 54 (2011) 940–954.

[30] H. Wang, J. W. Suh, S. R. Das, J. B. Pluta, C. Craige, P. A. Yushkevich, Multi-atlas segmentation with joint label fusion, IEEE Transactions on Pattern Analysis and Machine Intelligence 35 (2013) 611–623.

[31] M. Liu, A. Kitsch, S. Miller, V. Chau, K. Poskitt, F. Rousseau, D. Shaw, C. Studholme, Patch-based augmentation of Expectation-Maximization for brain MRI tissue segmentation at arbitrary age after premature birth, NeuroImage 127 (2016) 387–408.

[32] P. Coupé, P. Yger, S. Prima, P. Hellier, C. Kervrann, C. Barillot, An optimized blockwise nonlocal means denoising filter for 3-D magnetic resonance images, IEEE Transactions on Medical Imaging 27 (2008) 425–441.

[33] S. T. Roweis, L. K. Saul, Nonlinear dimensionality reduction by locally linear embedding, Science 290 (2000) 2323–2326.

[34] E. Hughes, L. Cordero-Grande, M. Murgasova, J. Hutter, A. Price, A. Santos Gomes, J. Allsop, J. Steinweg, N. Tusor, J. Wurie, J. Bueno-Conde, J.-D. Tournier, M. Abaei, S. Counsell, M. Rutherford, M. Pietsch, D. Edwards, J. Hajnal, S. Fitzgibbon, E. Duff, M. Bastiani, J. Andersson, S. Jbabdi, S. Sotiropoulos, M. Jenkinson, S. Smith, S. Harrison, L. Griffanti, R. Wright, J. Bozek, C. Beckmann, A. Makropoulos, E. Robinson, A. Schuh, J. Passerat Palmbach, G. Lenz, F. Mortari, T. Tenev, D. Rueckert, The Developing Human Connectome: Announcing the first release of open access neonatal brain imaging, in: OHBM, Procs., 2017.

[35] A. Makropoulos, E. C. Robinson, A. Schuh, R. Wright, S. Fitzgibbon, J. Bozek, S. J. Counsell, J. Steinweg, J. Passerat-Palmbach, G. Lenz, F. Mortari, T. Tenev, E. P. Duff, M. Bastiani, L. Cordero-Grande, E. Hughes, N. Tusor, J.-D. Tournier, J. Hutter, A. N. Price, M. Murgasova, C. Kelly, M. A. Rutherford, S. M. Smith, A. D. Edwards, J. V. Hajnal, M. Jenkinson, D. Rueckert, The Developing Human Connectome Project: A minimal processing pipeline for neonatal cortical surface reconstruction, bioRxiv (2017) 125526.

[36] B. B. Avants, C. L. Epstein, M. Grossman, J. C. Gee, Symmetric diffeo-morphic image registration with cross-correlation: Evaluating automated labeling of elderly and neurodegenerative brain, Medical Image Analysis 12 (2008) 26–41.

[37] J. Ashburner, K. J. Friston, Unified segmentation, NeuroImage 26 (2005) 839–851.

[38] D. Geffroy, D. Rivière, I. Denghien, N. Souedet, S. Laguitton, Y. Cointepas, BrainVISA: A complete software platform for neuroimaging, in: Python in Neuroscience Workshop, Procs., 2011.